Acta Materialia 159 (2018) 65–76

Contents lists available at ScienceDirect

Acta Materialia

journal homepage: www.elsevier.com/locate/actamat

Full length article

# Structural characteristics of $\{\bar{1}012\}$ non-cozone twin-twin interactions in magnesium

Mingyu Gong [a], Shun Xu [a], Yanyao Jiang [b], Yue Liu [c, **], Jian Wang [a, d, *]

[a] Mechanical and Materials Engineering, University of Nebraska-Lincoln, Lincoln, NE, 68588, USA
[b] Department of Mechanical Engineering, University of Nevada, Reno, NV, 89557, USA
[c] State Key Lab of Metal Matrix Composites, School of Materials Science and Engineering, Shanghai Jiaotong University, Shanghai, 200240, People's Republic of China
[d] Nebraska Center for Materials and Nanoscience, University of Nebraska-Lincoln, Lincoln, NE, 68588, USA

ARTICLE INFO

*Article history:*
Received 29 March 2018
Received in revised form
3 August 2018
Accepted 3 August 2018
Available online 6 August 2018

*Keywords:*
Twin-twin boundaries
Non-cozone twin-twin interactions
Structural characters
Magnesium

ABSTRACT

Twin-twin interactions form twin-twin boundaries (TTBs) which can prevent twin propagation, inhibit direct twin transmission, retard detwinning, and facilitate secondary twins. The current work studies the microstructure and interaction mechanisms of non-cozone twin-twin junctions by combining electron back-scatter diffraction observations and atomistic simulations. Non-cozone twin-twin interactions are defined as the intersecting line of the two twins isn't parallel to one <$1\bar{2}10$> zone axis (a-axis) and include two types, Type II(a) ($T_2 \rightarrow T_1$) and Type II(b) ($T_3 \rightarrow T_1$), according to the crystallography of two interacting twins. For Type II(a) interaction, both statistical results of experimental observations and interfacial energy calculation confirm TTB formation on the obtuse side of the incoming twin instead of the acute side. However, for Type II(b) interaction, the growth of twins on both sides is impeded, although the TTB on the acute side possesses the lowest interfacial energy. Atomistic simulation demonstrates that, for Type II(a) twin-twin interactions, positive resolved shear stresses on the obtuse side favor $T_1$ and $T_2$ twinning, while negative resolved shear stresses on the acute side impede $T_1$ and $T_2$ twinning. For Type II(b), negative resolved shear stresses on both the acute and obtuse sides result in impediment of twinning on both sides. These results can be used in developing micro/macro-scale predictive models that deal with the role of multiple twins and twin variants during mechanical processing. The analytical and simulation methods can be generalized and applied to atomistic analysis in different material systems to further explain the hardening mechanisms associated with twin-twin interactions.



## 1. Introduction

Magnesium (Mg) alloys are the lightest structural metallic materials which can be used in transportation vehicles to reduce weight and to increase fuel efficiency [1,2]. Plastic deformation in Mg and its alloys is accommodated by both dislocation slips and twins [3–6]. Primary deformation mechanisms at room temperature include basal <$\boldsymbol{a}$> slip ($\{0\,0\,0\,1\}\langle 1\,1\,\bar{2}\,0\rangle$) [7–9] and $\{1\,0\,\bar{1}\,2\}\langle\bar{1}\,0\,1\,1\rangle$ tension twin [7]. Prismatic <$\boldsymbol{a}$> slip $\{1\,0\,\bar{1}\,0\}\langle 1\,1\,\bar{2}\,0\rangle$ [7–9] and pyramidal $\langle\boldsymbol{a}+\boldsymbol{c}\rangle$ slip $\{1\,1\,\bar{2}\,2\}\langle\bar{1}\,\bar{1}\,2\,3\rangle/\{1\,0\,\bar{1}\,1\}\langle\bar{1}\,\bar{1}\,2\,3\rangle$ [7–10] are difficult to activate due to the low mobility of the associated dislocations with non-planar core. Tension twins $\{1\,0\,\bar{1}\,2\}\langle\bar{1}\,0\,1\,1\rangle$ are commonly observed [7]. $\{\bar{1}\,0\,1\,1\}$ and $\{\bar{1}\,0\,1\,3\}$ compression twins are theoretically possible but rarely occur at room temperature [11,12]. Multiple twin variants can be activated simultaneously and interact with each other. The phenomenon associated with a twin variant meeting another twin variant during deformation is referred to as twin-twin interaction. Twin-twin interactions result in various microstructures such as twin-twin junctions (TTJs) [13–16], compression-tension double twin [17–20], tension-tension double twin (or secondary tension twin) [13,21–23], and tension-

* Corresponding author. Mechanical and Materials Engineering, University of Nebraska-Lincoln, Lincoln, NE, 68588, USA.
** Corresponding author.
*E-mail addresses:* yliu23@sjtu.edu.cn (Y. Liu), jianwang@unl.edu (J. Wang).

https://doi.org/10.1016/j.actamat.2018.08.004
1359-6454/

compression-tension tertiary twin [23,24]. TTJs affect subsequent twinning, de-twinning, and slips during plastic deformation [13,14,25,26]. For instance, Sim et al. [27] reported an increase in strain hardening for single crystals and ascribed the increase to twin-twin and dislocation-twin interactions. Also, TTJ associated with two primary $\{1\,1\,\bar{2}\,1\}$ tension twins in titanium stimulates sequential $\{1\,0\,\bar{1}\,2\}$ twinning [28]. The local stresses created by twin-twin interactions further affect twin growth until it can be relaxed by plastic deformation. Local lattice distortion was found to relieve the stress induced by twin-twin interactions in zinc [29]. Roberts and Partridge [30] investigated the accommodation occurring around the intersected $\{1\,0\,\bar{1}\,2\}$ twins in Mg. It was found that the stress caused by twin-twin interactions was relaxed through producing kink bands within the blocked twins. Peng et al. [31] recently achieved a new double contraction twin structure by high-pressure technique, accounting for high strength of Mg alloys, and it might provide a new trajectory to the enhanced other hcp-type alloys. Rajan [32] examined the twin-twin interaction in Co–Cr–Mo alloy and attributed the formation of secondary twins to high localized stress. Mahajan and Chin [33] observed that the strain accommodation required for crossing twins in Co–Fe alloy was accomplished by secondary twinning inside the crossed twins and by slips. Co-zone $\{1\,0\,\bar{1}\,2\}$ TTJ facilitates basal slip band during loading and enhances secondary tension twinning during reversible loading [13]. The secondary twins constrained by the primary twin are difficult to be detwinned during cyclic loading, which leads twinning-induced strain hardening [13,25,26,34]. Recently, Alkan et al. [35] determined the latent hardening response of twin-twin interactions in a FeNiCoCrMn alloy. The accommodation mechanism associated with twin-twin interactions was studied in experiments mainly by using scanning electron microscope (SEM) and transmission electron microscopy (TEM). Little efforts have been made in the quantitative analysis on the effect of the local stress resulting from twin-twin interactions on the growth of the intersected twins.

To facilitate the discussion of $\{\bar{1}\,0\,1\,2\}$ twin-twin interaction, six equivalent $\{\bar{1}\,0\,1\,2\}$ twin variants are denoted as $T_i$ ($i = 1 \ldots 6$) (Fig. 1). The subscript changes from 1 to 6 following a counter-clockwise rotation about the <***c***>. The twin-twin interaction between an incoming $T_i$ and an encountering $T_j$ is denoted as $T_i \rightarrow T_j$ [13]. Twin-twin interactions are classified into two types according to the shared axis. Type I twin-twin interaction refers to co-zone $T_i \rightarrow T_{i\pm3}$ interaction because the two twin variants share the same <***a***> axis. Type II is non-cozone twin-twin interaction including Type II(a) $T_i \rightarrow T_{i\pm1}$ (Fig. 1(a)) and Type II(b) $T_i \rightarrow T_{i\pm2}$ (Fig. 1(d)). Co-zone $\{\bar{1}\,0\,1\,2\}$ twin-twin interaction has been investigated using atomistic simulations [25] and characterized using microscopes [13,36–38]. Two twin-twin boundaries (TTBs) associated with Type I TTJ were identified to have the habit planes $(1\,0\,\bar{1}\,0)$ and $(0\,0\,0\,1)$, corresponding to the prismatic||prismatic (PP) and basal||basal (BB) boundaries, respectively. Boundary dislocations are piled up along the habit plane of the TTB. The boundary dislocation $\mathbf{b}^{PP}$ on the PP boundary has the Burgers vector $2\lambda[0\,0\,0\,\bar{1}]$ and $\mathbf{b}^{BB}$ on the BB boundary has the Burgers vector $2\lambda[1\,0\,\bar{1}\,0]$, where $\lambda = 0.0649$ for Mg. These dislocations result in a tilt angle 7.4° to compensate the deviation angle between the habit planes in the two twins. Molecular dynamics (MD) simulations demonstrated the formation of the two TTBs and revealed their effect on slip, twinning, and detwinning at the atomic level [25,36,39]. For instance, basal slip bands are easily activated across the PP boundary because the basal planes are approximately parallel in the two twin variants. For non-cozone $\{\bar{1}\,0\,1\,2\}$ twin-twin interaction, Yu et al. [13] reported possible structures based on crystallographic analysis. Further characterizations from experimental observations and atomic level modeling are needed for a comprehensive understanding of twin-twin interactions. In addition, the analytical and simulation methods could be generalized and applied to atomistic analysis in different material systems to further explain the hardening mechanisms associated twin-twin interactions.

In the current study, microstructures of non-cozone TTJs in Mg are characterized based on electron backscatter diffraction (EBSD) observations. Structural characteristics of TTJs associated with twin-twin interaction are explored via molecular dynamics (MD) simulations. A statistical analysis of the structures of TTJs indicates that, for Type II(a) interaction, TTB forms on the obtuse side of the incoming twin, implying that the growth of two twins is favored on the obtuse side while impeded on the acute side. However, for Type II(b) interaction, incoming twin is blocked by the encountering twin, and the growth of both twins seems impeded. By using atomistic simulations, we study the structural characteristics based on the dislocation reactions and local stress fields associated with

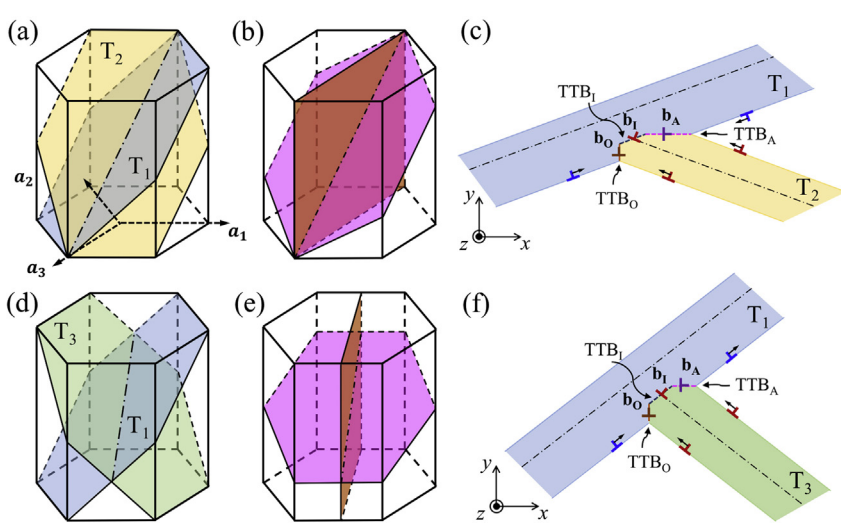


**Fig. 1.** (a) Type II(a) twin-twin pair $T_2 \rightarrow T_1$ with the interaction line along $[\bar{2}\,\bar{2}\,4\,\bar{3}]_M$. (b) $TTB_O$ (brown) and $TTB_A$ (pink) formed respectively on obtuse and acute sides of $T_2 \rightarrow T_1$ pair. (c) Schematics of $T_2 \rightarrow T_1$ junction including $TTB_O$, $TTB_A$ and $TTB_I$. (d) Type II(b) twin-twin pair $T_3 \rightarrow T_1$ with the interaction line along $[0\,\bar{2}\,2\,\bar{1}]_M$. (e) $TTB_O$ (brown) and $TTB_A$ (pink) formed respectively on obtuse and acute sides of the $T_3 \rightarrow T_1$ pair. (f) Schematics of $T_3 \rightarrow T_1$ junction with $TTB_O$, $TTB_A$ and $TTB_I$. (For interpretation of the references to colour in this figure legend, the reader is referred to the Web version of this article.)

the formation of TTJs. The results provide an insight into understanding non-cozone $\{\bar{1}\,0\,1\,2\}$ twin-twin interactions.

## 2. Structures of twin-twin junctions

### 2.1. Crystallographic analysis of TTJs

When $T_i \rightarrow T_j$ interaction occurs, TTB forms on the bisection plane between the primary twinning planes of $T_i$ and $T_j$. According the angle between the primary twinning planes of $T_i$ and $T_j$, $TTB_O$ is used to denote the TTB formed on the obtuse side and $TTB_A$ is used to represent the TTB formed on the acute side. In addition, $TTB_I$ denotes the case when the TTB is parallel to the twinning plane of the encountering twin.

For Type II(a) TTJs, the two twining planes of $T_1$ and $T_2$ and their intersection line are shown in a hexagonal close packed (hcp) unit (Fig. 1(a)). According to the crystallography of the two twins, the intersection line is along $[\bar{2}\,\bar{2}\,4\,\bar{3}]_M$. $TTB_O$ (the brown plane in Fig. 1(b)) is parallel to $(1\,\bar{1}\,0\,0)_M$ plane in the matrix while $TTB_A$ (the pink plane in Fig. 1(b)) is parallel to $(\bar{1}\,\bar{1}\,2\,4)_M$ plane in the matrix. $TTB_I$ is parallel to $(\bar{1}\,0\,1\,2)_M$ plane in the matrix. When the TTBs are described in the twin orientation (see appendix), $TTB_O$ is parallel to $(\bar{9}\,19\,\overline{10}\,18)_{T_1}$ plane in $T_1$ and $(\overline{19}\,9\,10\,\overline{18})_{T_2}$ plane in $T_2$. $TTB_A$ is parallel to $(31\,20\,\overline{51}\,62)_{T_1}$ plane in $T_1$ and $(20\,30\,\overline{51}\,62)_{T_2}$ plane in $T_2$. $TTB_I$ is parallel to $(\bar{1}\,0\,1\,2)_{T_1}$ plane in $T_1$ and $(15\,8\,\overline{23}\,\overline{16})_{T_2}$ plane in $T_2$. Fig. 1(c) shows a schematic configuration of $T_2 \rightarrow T_1$ TTJ, where the x- and y-directions are normal to $TTB_O$ and $TTB_A$, respectively, and the z-direction is along the intersection line. Twin dislocations (TDs) associated with $T_1$ and $T_2$ react and form boundary dislocations on the TTBs. $\mathbf{b_O}$ and $\mathbf{b_A}$, respectively, are used to denote the Burgers vectors of boundary dislocations on the two boundaries $TTB_O$ and $TTB_A$. $\mathbf{b_O}$ and $\mathbf{b_A}$ are equal to the sum of the Burgers vectors of TDs of $T_1$ and $T_2$. $TTB_I$ forms as TDs associated with $T_2$ pile up on coherent twin boundary of $T_1$. The Burgers vector $\mathbf{b_I}$ is equal to that of the TD of $T_2$. The Burgers vector of a TD $\boldsymbol{b_t}^{T_1}$ is equal to $\lambda[1\,0\,\bar{1}\,1]$ where $\lambda = 0.0649$. Setting the line sense of both TDs along $[\bar{2}\,\bar{2}\,4\,\bar{3}]_M$, the reactions of TDs associated with the formation of TTBs can be expressed as follows.

$$\begin{aligned} &\boldsymbol{b_t}^{T_1} - \boldsymbol{b_t}^{T_2} \Rightarrow \boldsymbol{b_O} \\ &\lambda\left[1\,0\,\bar{1}\,1\right] - \lambda\left[0\,1\,\bar{1}\,1\right] \Rightarrow \lambda\left[1\,\bar{1}\,0\,0\right] \end{aligned} \tag{1}$$

$$\begin{aligned} &\boldsymbol{b_t}^{T_1} + \boldsymbol{b_t}^{T_2} \Rightarrow \boldsymbol{b_A} \\ &\lambda\left[1\,0\,\bar{1}\,1\right] + \lambda\left[0\,1\,\bar{1}\,1\right] \Rightarrow \lambda\left[1\,1\,\bar{2}\,2\right] \end{aligned} \tag{2}$$

$$\begin{aligned} &\boldsymbol{b_t}^{T_2} \Rightarrow \boldsymbol{b_I} \\ &\lambda\left[0\,1\,\bar{1}\,1\right] \Rightarrow \lambda\left[0\,1\,\bar{1}\,1\right] \end{aligned} \tag{3}$$

Fig. 1(d) shows the two twin planes of $T_1$ and $T_3$ and the intersection line for a Type II(b) TTJ. The intersection line is along $[0\,\bar{2}\,2\,\bar{1}]_M$. $TTB_O$ (the brown plane in Fig. 1(e)) is parallel to $(2\,\bar{1}\,\bar{1}\,0)_M$ plane in the matrix while $TTB_A$ (the pink plane in Fig. 1(e)) is parallel to $(0\,\bar{1}\,1\,4)_M$ plane in the matrix. $TTB_I$ is parallel to $(\bar{1}\,0\,1\,2)_M$ plane in the matrix. With the operation described in appendix, $TTB_O$ is parallel to $(\bar{2}\,5\,\bar{3}\,14)_{T_1}$ plane in $T_1$ and $(\bar{2}\,\bar{3}\,5\,\overline{14})_{T_3}$ plane in $T_3$. $TTB_A$ is parallel to $(8\,5\,\overline{13}\,\bar{6})_{T_1}$ plane in $T_1$ and $(\bar{8}\,13\,\bar{5}\,\bar{6})_{T_3}$ plane in $T_3$. $TTB_I$ is parallel to $(\bar{1}\,0\,1\,2)_{T_1}$ plane in $T_1$ and $(\bar{3}\,8\,\bar{5}\,4)_{T_3}$ plane in $T_3$. A schematic illustration of $T_3 \rightarrow T_1$ TTJ is shown in Fig. 1(f), where the x- and y-directions are normal to $TTB_O$ and $TTB_A$ respectively, and the z-direction is along the intersection line $[0\,\bar{2}\,2\,\bar{1}]_M$. Setting the line sense of both TDs along $[0\,\bar{2}\,2\,\bar{1}]_M$, the reaction process can be expressed as:

$$\begin{aligned} &\boldsymbol{b_t}^{T_1} - \boldsymbol{b_t}^{T_3} \Rightarrow \boldsymbol{b_O} \\ &\lambda\left[1\,0\,\bar{1}\,1\right] - \lambda\left[\bar{1}\,1\,0\,1\right] \Rightarrow \lambda\left[2\,\bar{1}\,\bar{1}\,0\right] \end{aligned} \tag{4}$$

$$\begin{aligned} &\boldsymbol{b_t}^{T_1} + \boldsymbol{b_t}^{T_3} \Rightarrow \boldsymbol{b_A} \\ &\lambda\left[1\,0\,\bar{1}\,1\right] + \lambda\left[\bar{1}\,1\,0\,1\right] \Rightarrow \lambda\left[0\,1\,\bar{1}\,2\right] \end{aligned} \tag{5}$$

$$\begin{aligned} &\boldsymbol{b_t}^{T_3} \Rightarrow \boldsymbol{b_I} \\ &\lambda\left[\bar{1}\,1\,0\,1\right] \Rightarrow \lambda\left[\bar{1}\,1\,0\,1\right] \end{aligned} \tag{6}$$

According to theory of dislocations, the elastic energy of a dislocation is proportional to the square of the magnitude of its Burgers vector. The elastic energy of $\boldsymbol{b_t}^{T_1}$, $\boldsymbol{b_t}^{T_2}$ and $\boldsymbol{b_t}^{T_3}$ is proportional to $|\mathbf{b}_t|^2$. For the reactions expressed by Eqs. (1), (2), (4) and (5), two TDs react and form one boundary dislocation. The elastic energy of the dislocations on the left side of the equations is the sum of the elastic energy of two TDs, which is proportional to $2|\mathbf{b}_t|^2$. The elastic energy of the dislocation on the right side of the equations is proportional to $|\mathbf{b_A}|^2$ or $|\mathbf{b_O}|^2$. According to Frank's law [40], if the value of $|\mathbf{b_A}|^2/(2|\mathbf{b}_t|^2)$ or $|\mathbf{b_O}|^2/(2|\mathbf{b}_t|^2)$ is less than 1, the reaction is energetically favorable, and vice versa. In Eqs. (3) and (6), $\mathbf{b_I}$ has the same Burgers vector and elastic energy of either $\boldsymbol{b_t}^{T_2}$ or $\boldsymbol{b_t}^{T_3}$. The value of $|\mathbf{b_I}|^2/|\mathbf{b}_t|^2$ is 1. Table 1 shows the Burgers vectors of $\mathbf{b_I}$, $\mathbf{b_A}$ and $\mathbf{b_O}$ in Eqs. (1)–(3) and Eqs. (4)–(6) as well as the value of $|\mathbf{b_I}|^2/|\mathbf{b}_t|^2$, $|\mathbf{b_A}|^2/(2|\mathbf{b}_t|^2)$ and $|\mathbf{b_O}|^2/(2|\mathbf{b}_t|^2)$'. It's found that the values of $|\mathbf{b_A}|^2/(2|\mathbf{b}_t|^2)$ for both $T_2 \rightarrow T_1$ and $T_3 \rightarrow T_1$ pairs are larger than 1 while those of $|\mathbf{b_O}|^2/(2|\mathbf{b}_t|^2)$ for both pairs are smaller than 1, suggesting the formation of $TBB_O$ is energetically favorable while $TTB_A$ is unfavorable.

### 2.2. Experimental characterization of TTJs

We characterized TTJs in a deformed polycrystalline Mg specimen. An extruded commercially pure and fully recrystallized polycrystalline Mg rod with a strong basal texture was subjected to tension-compression cyclic loading at a strain magnitude of 1%. Standard metallographic techniques were used to polish specimens. An FEI XL30 with an accelerating voltage of 25 kV was used for EBSD scanning to obtain crystal orientation for both parent and twin phases.

Structural feature of a TTJ was characterized by a geometrical analysis method based on traces of boundary planes on the observed surface and corresponding pole figures. Because the normal of the observed surface is along an arbitrary crystallographic direction, we first define the trace of a boundary plane on the observed surface according to EBSD data, followed by the use of a pole figure to determine which crystallographic plane is a best fit for the trace [15]. As illustrated in Fig. 2(a), two planes, $P_i$ $(h_i\,k_i\,i_i\,l_i)$ and $P_j$ $(h_j\,k_j\,i_j\,l_j)$, intersect. The angle $\theta_{ij}$ between the two planes is calculated by

$$\theta_{ij} = cos^{-1}\left(h_ih_j + k_ik_j + \frac{1}{2}(h_ik_j + h_jk_i) + \frac{3a^2}{4c^2}l_il_j \Big/ \sqrt{\left(h_i^2 + k_i^2 + h_ik_i + \frac{3a^2}{4c^2}l_j^2\right)\left(h_i^2 + k_i^2 + h_jk_j + \frac{3a^2}{4c^2}l_j^2\right)}\right) \tag{7}$$

**Table 1**
Dislocations associated with the formation of TTBs associated with non-cozone twin-twin interactions.

| Pair | $\mathbf{b}_I$ | $\mathbf{b}_A$ | $\mathbf{b}_O$ | $\lvert\mathbf{b}_I\rvert^2/\lvert\mathbf{b}_t\rvert^2$ | $\lvert\mathbf{b}_A\rvert^2/(2\lvert\mathbf{b}_t\rvert^2)$ | $\lvert\mathbf{b}_O\rvert^2/(2\lvert\mathbf{b}_t\rvert^2)$ |
|---|---|---|---|---|---|---|
| $\mathbf{T}_2\rightarrow\mathbf{T}_1$ | $\lambda[0\,1\,\bar{1}\,1]$ | $\lambda[1\,1\,\bar{2}\,2]$ | $\lambda[1\,\bar{1}\,0\,0]$ | 1.00 | 1.74 | 0.27 |
| $\mathbf{T}_3\rightarrow\mathbf{T}_1$ | $\lambda[\bar{1}\,1\,0\,1]$ | $\lambda[0\,1\,\bar{1}\,2]$ | $\lambda\left[2\,\bar{1}\,\bar{1}\,0\right]$ | 1.00 | 1.21 | 0.80 |

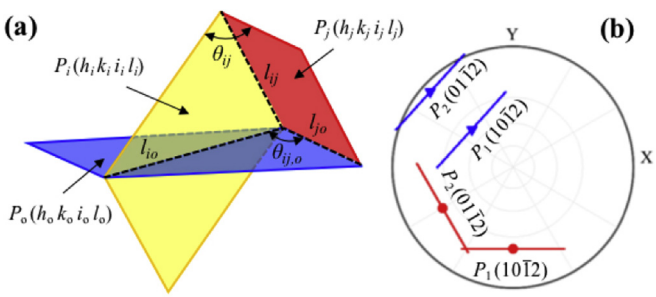


**Fig. 2.** (a) Angle between two twin planes of twins $T_i^I$ (yellow) and $T_j^I$ (red) on the observed plane $P_O$ (blue); (b) Illustration of pole figure showing variation of the traces of two twin planes with the observed plane:red lines represent the traces of $P_1 = (1\,0\,\bar{1}\,2)$ and $P_2 = (0\,1\,\bar{1}\,2)$ on the observed plane $P_O = (0\,0\,0\,2)$, and blue lines are the traces of $P_1$ and $P_2$ on the observed plane $P_O = (\bar{1}\,1\,0\,0)$. (For interpretation of the references to colour in this figure legend, the reader is referred to the Web version of this article.)

Since the measured angle between the traces of the two planes on an observed surface varies with the normal of the observed surface, the trace of $P_i$ on $P_o$ is given by the following expression on an observed surface $P_o$ $(h_o\ k_o\ i_o\ l_o)$,

$$l_{io} = \left[\frac{a}{c}k_i l_o - \frac{a}{c}k_o l_i,\ \frac{\sqrt{3}a}{3c}l_i(2h_o + k_o) - \frac{\sqrt{3}a}{3c}l_o(2h_i + k_i), \frac{2\sqrt{3}a}{3c}h_i k_o - \frac{2\sqrt{3}a}{3c}h_o k_i\right] \tag{8}$$

The trace of $P_j$ on $P_o$ is given by:

$$l_{jo} = \left[\frac{a}{c}k_j l_o - \frac{a}{c}k_o l_j,\ \frac{\sqrt{3}a}{3c}l_j(2h_o + k_o) - \frac{\sqrt{3}a}{3c}l_c(2h_j + k_j), \frac{2\sqrt{3}a}{3c}h_j k_o - \frac{2\sqrt{3}a}{3c}h_o k_j\right] \tag{9}$$

The angle $\theta_{ij,o}$ between the two traces is given by:

$$\theta_{ij,o} = cos^{-1}\left(\frac{l_{io} \cdot l_{jo}}{|l_{io}||l_{jo}|}\right) \tag{10}$$

In Eq. (10), $\theta_{ij,o}$ represents the measured angle between two planes $P_i$ and $P_j$ on the observed surface $P_o$. As illustrated in Fig. 2(b), the pole figure has Y || the intersection line between the observed surface and (0 0 0 2) plane, Z || the normal of the observed plane, and X = Y × Z. For two twin planes, $P_1$ $(1\,0\,\bar{1}\,2)$ and $P_2$ $(0\,1\,\bar{1}\,2)$, in Mg, the angle $\theta_{12}$ is 40°. If the observed surface $P_o$ is (0 0 0 2) plane, the red lines indicate the traces of two twin planes on the observed surface. Therefore, the measured angle $\theta_{12,o}$ is equal to 60°. When $P_o$ is $(\bar{1}\,1\,0\,0)$, $\theta_{12,o} = 0°$ since the two twin planes, $P_1$ and $P_2$, intersect with the observation plane $P_o$ along the same direction $[2\,2\,\bar{4}\,\bar{3}]$as shown by the blue lines in Fig. 2(b).

Structural features of TTJs are characterized statistically according to EBSD data using the geometrical analysis method. Once the twin variants are identified by using $\{\bar{1}\,0\,1\,2\}$ pole figures, the bisection planes between the two twinning planes are calculated and then plotted into a pole figure. The trace of the bisection planes where TTBs lie will be used to compare with the detected EBSD images, which is helpful for determining the production of TTBs. Fig. 3 shows a representative EBSD scan of a polycrystalline Mg sample after one full loading cycle with the projection of [001] axis. To reveal the details of the intersected twins, two areas (black dashed boxes) in Fig. 3 are enlarged and are shown in Fig. 4. Fig. 4(a) contains a Type II(a) TTJ. The two twin variants, $T_1$ and $T_2$, are identified with the help of the pole figure shown in Fig. 4(b) where the red and blue dashed lines are the traces of two twinning planes. The bisection planes between $T_1$ and $T_2$ twinning planes are $(1\,1\,\bar{2}\,4)$ and $(\bar{1}\,1\,0\,0)$ on the acute and obtuse sides, respectively. The projection of the bisection planes containing TTBs is shown in Fig. 4(c), and the result indicates the formation of $TTB_O$. In addition, $T_1$ is thicker on the obtuse side than the acute side.

Another Type II(b) TTJ is shown in Fig. 4(d). The traces of the $T_1$ and $T_3$ twinning planes are marked by red and blue dashed lines, respectively, and these traces are consistent with those shown in the pole figure (Fig. 4(e)). The bisection planes between $T_1$ and $T_3$ twinning planes are $(0\,1\,\bar{1}\,4)$ and $(\bar{2}\,1\,1\,0)$ on the acute and obtuse side, respectively, which are also shown in the pole figure of TTBs (Fig. 4(f)). It is noticed that $TTB_I$ is produced, and there is no difference in thickness of $T_1$ on both sides of the incoming twin.

Three parameters, $\mathbf{t_I}$, $\mathbf{t_O}$, and $\mathbf{t_A}$, are used to describe the geometry of a TTJ, as schematically shown in Fig. 5(a) for both Type II(a) and Type II(b). $\mathbf{t_O}$ and $\mathbf{t_A}$ represent the thicknesses of the encountering twin variants on the obtuse and acute sides, respectively. Among 33 Type II(a) TTJs identified in the EBSD maps, we observed that $TTB_O$ can be clearly identified while $TTB_A$ are rarely

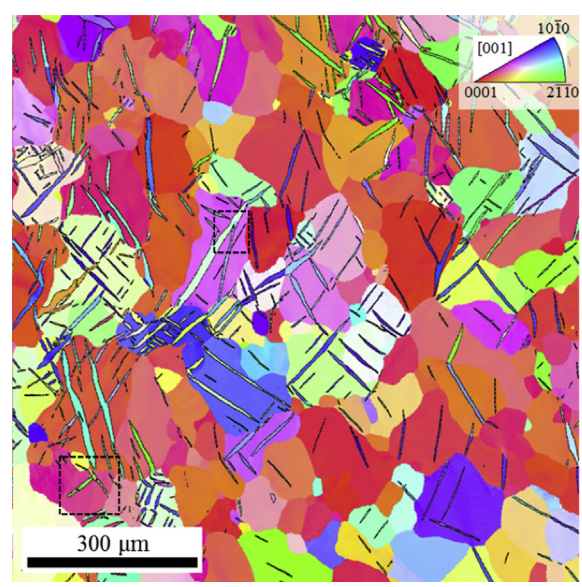


**Fig. 3.** Typical EBSD map of a polycrystalline Mg sample after cyclic loading in the extruded direction at 1% strain amplitude. Two regions are marked with dashed black boxes to be studied in detail.

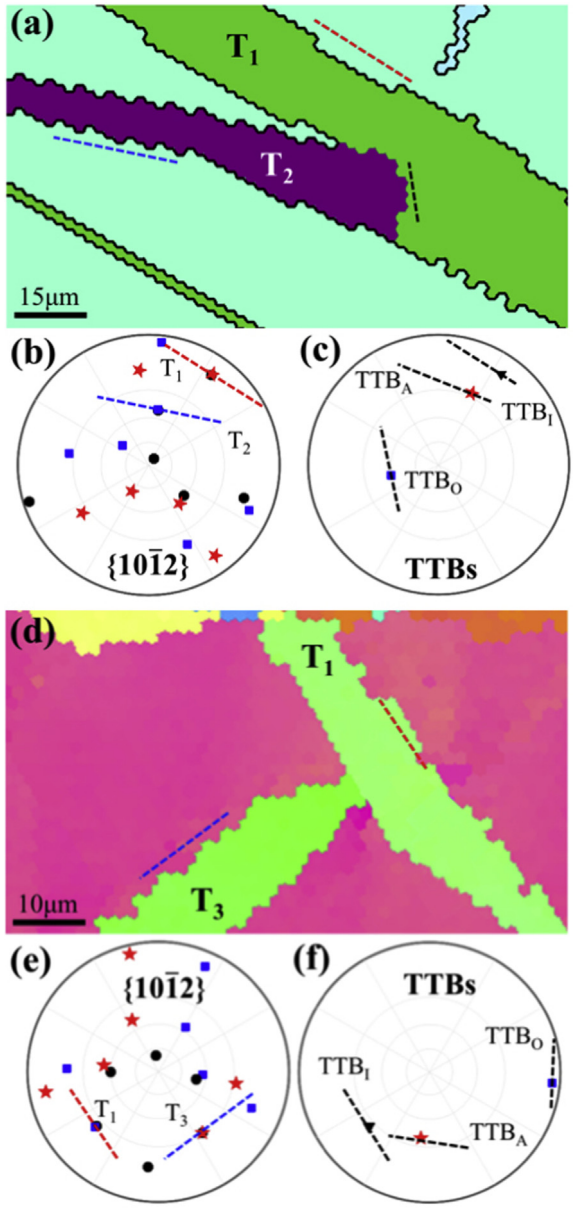


**Fig. 4.** (a) An example of Type II(a) twin-twin structure. (b) {1 0 $\bar{1}$ 2} pole figures of the grain and two twins in (a) with the traces of $TTB_A$ and $TTB_O$ being shown in (c). (d) An example of Type II(b) twin-twin structure. (e) {1 0 $\bar{1}$ 2} pole figures of the grain and two twins in (d), where the traces of $TTB_A$ and $TTB_O$ are shown in (f).

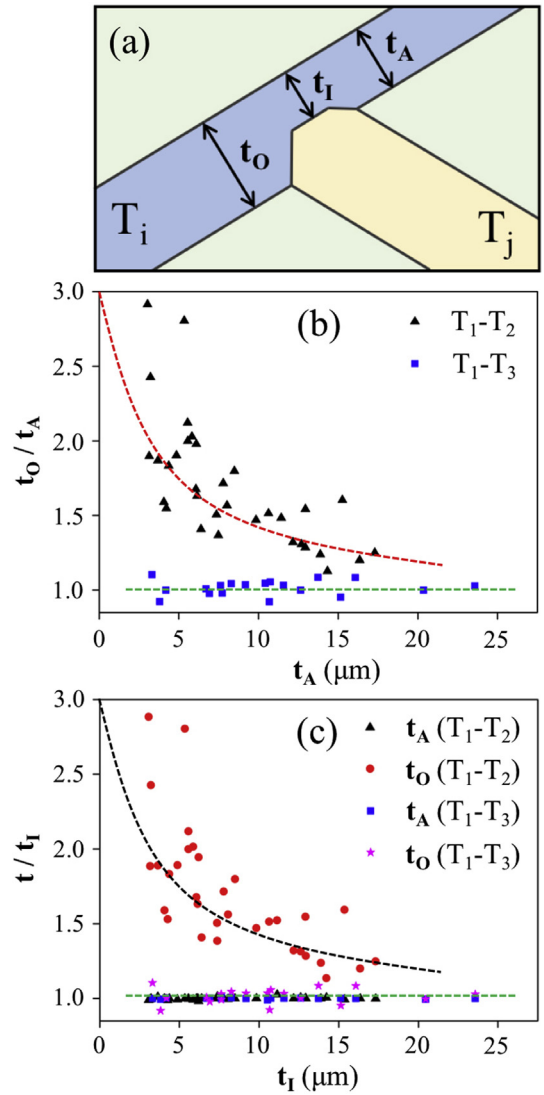


**Fig. 5.** (a) Schematic of $T_j \rightarrow T_i$ junction. (b) Variation of $\mathbf{t_O}/\mathbf{t_A}$ with $t_A$. (c) $\mathbf{t}/\mathbf{t_I}$ as function of $\mathbf{t_I}$.

detectable. The observation is corresponding to thickening both twins on the obtuse side of the TTJs while suppressing twin growth on the acute side of the TTJs. As a result, $\mathbf{t_O}$ is larger than $\mathbf{t_A}$. Among 17 identified Type II(b) TTJs, the twin thickness on the acute side is equal to that on the obtuse side, i.e., $\mathbf{t_O} = \mathbf{t_A}$. Neither $TTB_O$ nor $TTB_A$ is observed. Only $TTB_I$ can be clearly characterized from the EBSD image. The observation suggests that the formation of $TTB_I$ is preferred when $T_1$ and $T_3$ twins meet. Fig. 5(b) shows the variation of the ratio $\mathbf{t_O}/\mathbf{t_A}$ as a function of $\mathbf{t_A}$. For Type II(a) TTJs (black points), the ratio $\mathbf{t_O}/\mathbf{t_A}$ is always greater than unit, indicating that the encountering twin grows thicker on the obtuse side than that on the acute side. For Type II(b) TTJs (blue points), the ratio $\mathbf{t_O}/\mathbf{t_A}$ is approximately unit, suggesting that both sides of the encountering twin may have similar growth magnitude. Fig. 5(c) shows the growth magnitude of the encountering twin on the two sides. The result indicates that TTJs strongly impede the growth of the encountering twin.

## 3. Structure and energy of equilibrium TTBs

A dislocations-based elasticity theory speculates that $TTB_O$ are the prevalent boundaries in both Type II(a) and Type II(b) TTJs. Such a speculation contradicts with the experimental observations in Type II(b) TTJs. To address the discrepancy, in what follows, we will analyze structure and energy of the TTBs using atomistic simulations. Here we computed the formation energy of equilibrium boundaries. In order to prevent the relaxation process from being trapped in a local energy minimum, the relaxation of equilibrium TTB follows two steps [41]. First, two crystals are allowed to translate with respect to each other as rigid bodies in three dimensions to achieve the most favorable relative positions and interface spacing. A fine grid of 0.1 nm in both the x-direction and z-direction is applied with a boundary-unit-cell for the displacements on the x-z plane. Second, three configurations with the lowest energy from the first step are selected for further relaxation. During relaxation, all atoms are allowed to relax fully and

independently to reduce net force within the system. The final configuration with the lowest energy is taken as the structure of the equilibrium TTB.

The relaxed structures of $TTB_O$ and $TTB_A$ associated with Type II(a) interaction are shown in Fig. 6(a) and (b), respectively. $TTB_O$ boundary is $(\bar{1}\,2\,\bar{1}\,2)_{T_1}\|(\bar{2}\,1\,1\,\bar{2})_{T_2}$ semi-coherent interface comprising coherent $(\bar{1}\,2\,\bar{1}\,2)_{T_1}\|(\bar{2}\,1\,1\,\bar{2})_{T_2}$ interface and grain boundary dislocations (GBDs). The Burgers vector of the GBDs is equal to $(0,\ -0.27,\ 0)$ or $\left(0,\ 2d_{\{11\bar{2}2\}}\cos\frac{\phi}{2},\ 0\right)$ in the current coordinates, where $\phi = 5.1°$. The average distance between two neighboring GBDs is 3.1 nm, which is identical to the theoretical value. Fig. 6(b) shows the relaxed structure of $TTB_A$. Instead of forming semi-coherent $(3\,2\,\bar{5}\,6)_{T_1}\|(2\,3\,\bar{5}\,6)_{T_2}$ interface, a serrated interface comprises two terraced planes, $(\bar{1}\,0\,1\,2)$ twin plane in $T_1$ orientation and $(0\,\bar{1}\,1\,2)$ twin plane in $T_2$ orientation, and two types of GBDs. The Burgers vectors of the GBDs on $(\bar{1}\,0\,1\,2)$ plane and $(0\,\bar{1}\,1\,2)$ plane are $\beta[0\,1\,\bar{1}\,1]$ and $\beta[1\,0\,\bar{1}\,1]$ ($\beta = -0.4675$), respectively, with respect to the matrix orientation. The average distance between two GBDs is 4.1 nm which is close to the theoretical value of 4.0 nm. The interface energies are 242 mJ/m$^2$ for the $TTB_O$, 352 mJ/m$^2$ for $TTB_A$ and 340 mJ/m$^2$ for $TTB_I$. According to the energy criterion, equilibrium $TTB_O$ is more energetically favorable than $TTB_A$ and $TTB_I$ in Type II(a) TT interaction. This is consistent with the experiment observation.

The relaxed structures of $TTB_O$ and $TTB_A$ associated with Type II(b) TT interaction are shown in Fig. 6(c) and (d), respectively. The relaxed structure of $TTB_O$ is semi-coherent $(\bar{1}2\bar{1}6)_{T_1}\|(\bar{1}\bar{1}2\bar{6})_{T_3}$ interface containing equally spaced GBDs. The Burgers vector of the GBD is $(0,\ 0.08,\ 0)$ or $\left(0,\ 2d_{\{11\bar{2}6\}}\cos\frac{\phi}{2},\ 0\right)$ under the current coordinates, where $\phi = 7.5°$. The average distance between two nearby GBDs is 1.1 nm which is close to the theoretical value of 1.2 nm. Fig. 6(d) shows the atomic structure of $TTB_A$ that is semi-coherent $(12\,7\,\overline{19}\,\overline{10})_{T_1}\|(12\,\overline{19}\,7\,10)_{T_3}$ interface containing uniformly distributed GBDs. The Burgers vector of the GBD is $(0,\ 0.12,\ 0)$ or $\left(0,\ 2d_{\{12\,7\,\overline{19}\,\overline{10}\}}\cos\frac{\phi}{2},\ 0\right)$ under the current coordinate system, where $\phi = 4.1°$. The interface energies of $TTB_O$ and $TTB_A$ are 363 mJ/m$^2$ and 282 mJ/m$^2$, respectively. The interface energy of $TTB_I$ is 330 mJ/m$^2$. Based on the energy criterion, equilibrium $TTB_A$ is predicted to be more energetically favorable than $TTB_O$ in Type II(b) TT interaction. However, neither $TTB_O$ nor $TTB_A$ is observed in experiments. It should be noted that creating a boundary during mechanical deformation involves dynamics (i.e. formation process) and energetics (i.e. structural relaxation) processes. The dynamics process must precede the energetics process. Therefore, it is necessary to study the dynamics process of the twin-twin interactions.

## 4. MD simulations of non-cozone twin-twin interactions

### 4.1. Type II(a) twin-twin interaction

Deformation twins are introduced in a single crystal by successive gliding multiple TDs on every two atomic twin planes from the surface to the position of the twin tip. Atoms associated with the motion of TDs involve both the shear displacement (equal to Burgers vector) and shuffle displacement (defined in an exchange cell in Fig. 7) as discussed by Gong et al. [42]. Each deformation twin can be created in a crystal through two steps: 1) TDs are introduced in the crystal by the application of the anisotropic Barnett-Lothe solutions [43] for the displacement field of a dislocation; and 2) atoms in the twin domain are then displaced according to the shuffle vectors. The Burgers vector and associated shuffle vectors are determined in Fig. 7 by the e-cell. In the coordinate associated with $T_i$ (x-direction is along twinning direction of $T_i$, y-axis is normal to twinning plane of $T_i$ and z-axis is along zone direction of

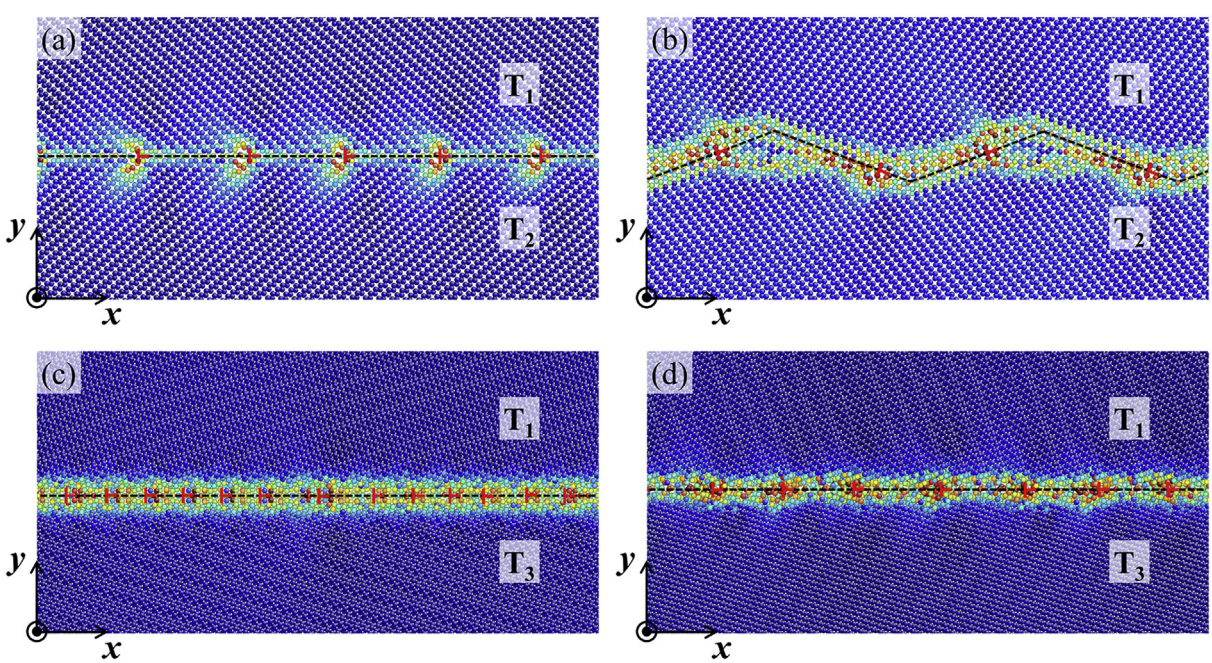


**Fig. 6.** Atomic structures of Type II(a) equilibrium $TTB_O$ (a) and $TTB_A$ (b), with y-direction normal to the TTB and z-direction along the intersection line $([\bar{2}\,\bar{2}\,4\,\bar{3}]_M)$. Atomic structures of Type II(b) equilibrium $TTB_O$ (c) and $TTB_A$ (d) with y-direction normal to the TTB and z-direction along the intersection line $([0\,\bar{2}\,2\,\bar{1}]_M)$.

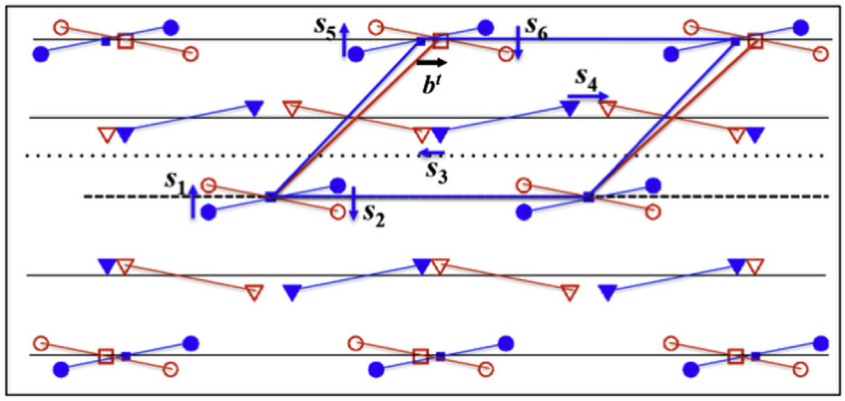


**Fig. 7.** Coherent dichromatic complex of $\{\bar{1}012\}$ twinning. Basis pairs connected by thin blue and red solid lines, dividing surface indicated by heavy dashed line, commensurate plane by dotted line. Black arrow indicates Burgers vector of TD and blue arrows indicate shuffle displacement. An e-cell is denoted by thick blue and red solid lines. (For interpretation of the references to colour in this figure legend, the reader is referred to the Web version of this article.)

**Table 2**
Burgers vectors and shuffle vectors associated with the two twins (Type II(a)) in the model coordinate.

| **Model coordinate**: x-direction along $[1\,\bar{1}\,0\,0]_M$, y-direction along the normal of $(\bar{1}\,\bar{1}\,2\,4)_M$ plane, and z-direction along $[\bar{2}\,\bar{2}\,4\,\bar{3}]_M$ | |
|---|---|
| **Twin $T_1$**: $(\bar{1}\,0\,1\,2)\,[1\,0\,\bar{1}\,1]$ | **Twin $T_2$**: $(0\,\bar{1}\,1\,2)\,[0\,1\,\bar{1}\,1]$ |
| $\boldsymbol{b}_t^{T_1} = (0.0178,\ 0.0065,\ -0.0450)$ nm | $\boldsymbol{b}_t^{T_2} = (-0.0178,\ 0.0065,\ -0.0450)$ nm |
| $\boldsymbol{s}_1^{T_1} = (-0.0108,\ 0.0296,\ 0)$ nm | $\boldsymbol{s}_1^{T_2} = (0.0108,\ 0.0296,\ 0)$ nm |
| $\boldsymbol{s}_2^{T_1} = (0.0108,\ -0.0296,\ 0)$ nm | $\boldsymbol{s}_2^{T_2} = (-0.0108,\ -0.0296,\ 0)$ nm |
| $\boldsymbol{s}_3^{T_1} = (-0.0156,\ -0.0057,\ 0.0394)$ nm | $\boldsymbol{s}_3^{T_2} = (0.0156,\ -0.0057,\ 0.0394)$ nm |
| $\boldsymbol{s}_4^{T_1} = (0.0336,\ 0.0122,\ -0.0848)$ nm | $\boldsymbol{s}_4^{T_2} = (-0.0336,\ 0.0122,\ -0.0848)$ nm |
| $\boldsymbol{s}_5^{T_1} = (-0.0108,\ 0.0296,\ 0)$ nm | $\boldsymbol{s}_5^{T_2} = (0.0108,\ 0.0296,\ 0)$ nm |
| $\boldsymbol{s}_6^{T_1} = (0.0108,\ -0.0296,\ 0)$ nm | $\boldsymbol{s}_6^{T_2} = (-0.0108,\ -0.0296,\ 0)$ nm |

$T_i$), Burgers vector is $\boldsymbol{b_t} = (0.0488,\ 0,\ 0)$ nm and shuffle vectors include $\boldsymbol{s}_1 = (0,\ 0.0315,\ 0)$ nm, $\boldsymbol{s}_2 = (0,\ -0.0315,\ 0)$ nm, $\boldsymbol{s}_3 = (-0.0427,\ 0,\ 0)$ nm, $\boldsymbol{s}_4 = (0.0920,\ 0,\ 0)$ nm, $\boldsymbol{s}_5 = (0,\ 0.0315,\ 0)$ nm and $\boldsymbol{s}_6 = (0,\ -0.0315,\ 0)$ nm.

The creation of Type II(a) twin-twin structure starts with an $80nm \times 80nm \times 1.6nm$ single crystal. The coordinates are x-direction along $[1\,\bar{1}\,0\,0]_M$, y-direction along the normal of $(\bar{1}\,\bar{1}\,2\,4)_M$ plane, and z-direction along $[\bar{2}\,\bar{2}\,4\,\bar{3}]_M$. Burgers vectors and shuffle vectors associated with $T_1$ and $T_2$ are listed in Table 2 in the model coordinate. With these vectors, we created two twins in the single crystal through two steps in the defined regions — introducing 20 TDs in each defined twin domain and displacing atoms in the twin domain with corresponding shuffle vectors. The thickness of both $T_1$ and $T_2$ twins is 7.6 nm. The intersection angle between the two twin planes is 40° or 140°.

When a dislocation is introduced in a single crystal by the application of the anisotropic Barnett-Lothe solutions [43] for the displacement field of a dislocation, the elastic field associated with the dislocation is approximately equilibrium while the local fields around the dislocation core is non-equilibrium because the elastic field does not describe the non-linear effect in the dislocation core. In atomistic simulation, a twin is created by successive introducing twinning dislocations by the application of the anisotropic Barnett-Lothe solutions [43]. The twin structure is nearly equilibrium. The twin tip contains multiple TDs and further relaxation is needed. With fixed boundary condition in x- and y-direction and periodic boundary condition in z-direction, the created twin structure was relaxed by dynamic quenching technique for 2 pico-seconds. After that, molecular dynamics simulation was conducted at 10 K with gradually increasing the applied strains. Twin $T_2$ exhibits a relatively stable structure at the applied stress $\mathbf{S_0}$

$$\mathbf{S}_0 = \begin{pmatrix} -0.11 & 0 & 0 \\ 0 & 0.11 & -0.40 \\ 0 & -0.40 & 0 \end{pmatrix} \text{GPa} \tag{11}$$

which generates the resolved shear stresses of 380 MPa on the two twinning planes. When the applied stress increases from $\mathbf{S_0}$ to $\mathbf{S_1}$

$$\mathbf{S}_1 = \begin{pmatrix} -0.15 & 0 & 0 \\ 0 & 0.15 & -0.53 \\ 0 & -0.53 & 0 \end{pmatrix} \text{GPa} \tag{12}$$

which generates a resolved shear stress of 500 MPa on the two twinning planes, $T_2$ twin propagates towards $T_1$ twin. Consequently, two TTBs, $TTB_I$ and $TTB_O$, are formed as shown in Fig. 8. It is observed that at the initial stage of twin-twin interaction, TDs associated with $T_2$ twinning are blocked by the coherent twin boundary of $T_1$ and form $TTB_I$. Thereafter, $TTB_O$ is created through the nucleation and emission of TDs associated with $T_1$ twin. The process can be ascribed to the dissociation of TDs associated with $T_2$ twinning on the $T_1$ twin plane, as described in a crystallographic model [13]. Correspondingly, $TTB_O$ can be considered as the pileup of the residual dislocations that have the Burgers vector $\mathbf{b_O}$ ($\lambda[1\,\bar{1}\,0\,0]$) defined in Eq. (1). The $TTB_O$ plane is parallel to $(1\,\bar{1}\,0\,0)_M$. It is noticed that $TTB_A$ does not form. When increasing the applied resolved shear stress to 700 MPa, $TTB_O$ boundary apparently extends but $TTB_A$ does not appear (Fig. 8(c)). These MD simulation results are consistent with the experimental observations (Fig. 3(b)).

The local stress near a TTJ can be relaxed in multiple ways such as growth/propagation of twins [42,44–47] and nucleation and emission of lattice dislocations [42,48–52]. The difference in the

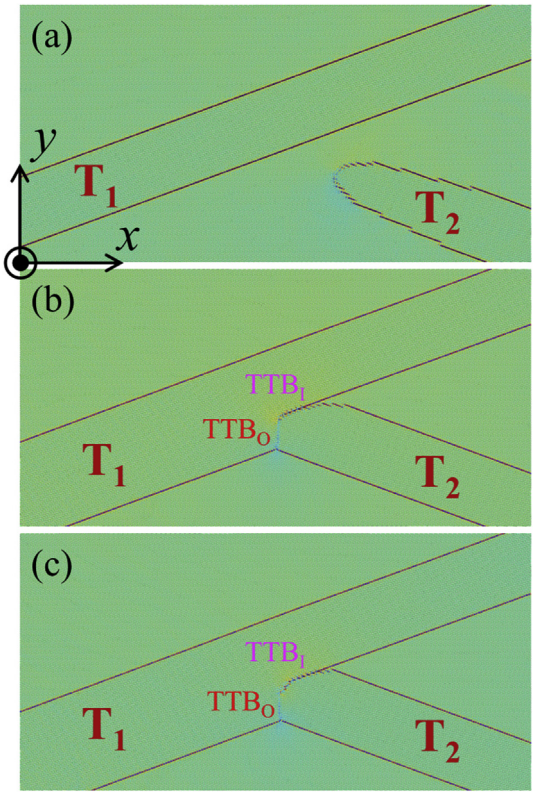


**Fig. 8.** (a) Initial Type II(a) $T_2 \rightarrow T_1$ structure. Final structures of $T_2 \rightarrow T_1$ interaction under the resolved shear stress of (b) 500 MPa (b) and (c) 700 MPa.

dissociation of TDs between two sides of the incoming twin $T_2$ can be understood according to the local stresses. We thus calculated the resolved shear stresses associated with TDs on the two twin planes on both sides of the incoming twin $T_2$ as well as the three <***a***> dislocations on basal plane in the encountering twin $T_1$. Fig. 9(a) and 9(b) show the stress fields of the resolved shear stress $\tau^{T_1}$ and $\tau^{T_2}$, respectively, and Fig. 9(c) shows the distribution of shear stress $\tau^b$ on the basal plane. Fig. 9(d) depicts the variation of $\tau^{T_1}$ and $\tau^{T_2}$ on the plane which is 1 nm away from the twin boundaries (TBs) (denoted by the arrows). It is clear that on the obtuse side both $\tau^{T_1}$ and $\tau^{T_2}$ have positive values, favoring $T_1$ and $T_2$ twinning and the formation of $TTB_O$. However, on the acute side, $\tau^{T_1}$ and $\tau^{T_2}$ have negative values. Hence, neither $T_1$ nor $T_2$ twin is facilitated to grow on the acute side, preventing the formation of $TTB_A$. These simulation results are consistent with experimental observation.

### 4.2. Type II(b) twin-twin interaction

To study Type II(b) twin-twin interactions, a single crystal slab with dimensions of $80nm \times 80nm \times 2.4nm$ is adopted. The model coordinate is x-direction along $[2\,\bar{1}\,\bar{1}\,0]_M$, y-direction along the normal of $(0\,\bar{1}\,1\,4)_M$ plane, and z-direction along $[0\,\bar{2}\,2\,\bar{1}]_M$. Burgers vectors and shuffle vectors associated with $T_1$ and $T_3$ are listed in Table 3 in the model coordinate. With these vectors, we created two twins in the single crystal through two steps in the defined regions — introducing 20 TDs in each defined twin domain and displacing atoms in the twin domain with corresponding shuffle vectors. The thickness of both $T_1$ and $T_3$ twins is 7.6 nm. The intersection angle between the two twin planes is 72° or 108°.

The created twin structure was relaxed by dynamic quenching technique for 2 pico-seconds. After that, molecular dynamics simulation was conducted at 10 K with gradually increasing the applied strains. Twin $T_3$ exhibits a relatively stable structure, as shown in Fig. 10(a), at the applied stress $\mathbf{S_0'}$

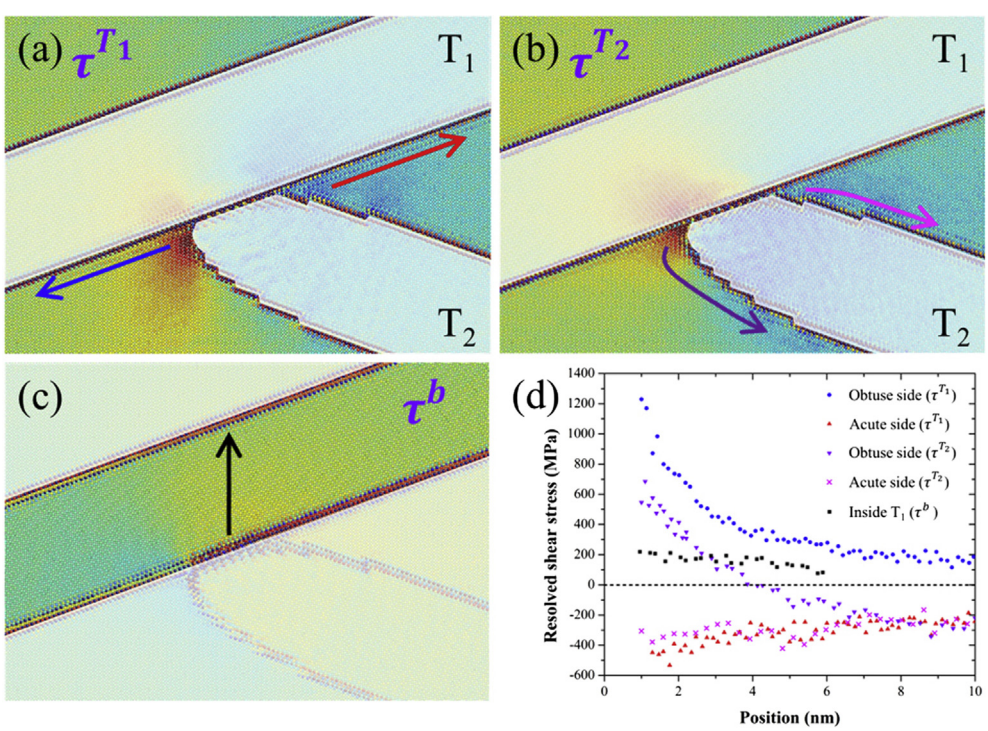


**Fig. 9.** (a)–(c) Stress fields of resolved shear stresses $\tau^{T_1}$ and $\tau^{T_2}$ and shear stress $\tau^b$ near Type II(a) TTJ. (d) Variations of resolved shear stresses $\tau^{T_1}$ and $\tau^{T_2}$ and shear stress $\tau^b$ on the planes near the TBs along the arrowed lines.

**Table 3**
Burgers vectors and shuffle vectors associated with the two twins (Type II(b)) in the model coordinate.

| **Model coordinate**: x-direction along $[2\,\bar{1}\,\bar{1}\,0]_M$, y-direction along the normal of $(0\,\bar{1}\,1\,4)_M$ plane, and z-direction along $[0\,\bar{2}\,2\,\bar{1}]_M$ | |
|---|---|
| **Twin $T_1$**: $(\bar{1}\,0\,1\,2)\,[1\,0\,\bar{1}\,1]$ | **Twin $T_3$**: $(1\,\bar{1}\,0\,2)\,[\bar{1}\,1\,0\,1]$ |
| $\boldsymbol{b}_t^{T_1} = (0.0308,\ 0.0227,\ -0.0303)$ nm | $\boldsymbol{b}_t^{T_3} = (-0.0308,\ 0.0227,\ -0.0303)$ nm |
| $\boldsymbol{s}_1^{T_1} = (-0.0187,\ 0.0254,\ 0)$ nm | $\boldsymbol{s}_1^{T_3} = (0.0187,\ 0.0254,\ 0)$ nm |
| $\boldsymbol{s}_2^{T_1} = (0.0187,\ -0.0254,\ 0)$ nm | $\boldsymbol{s}_2^{T_3} = (-0.0187,\ -0.0254,\ 0)$ nm |
| $\boldsymbol{s}_3^{T_1} = (-0.0270,\ -0.0198,\ 0.0265)$ nm | $\boldsymbol{s}_3^{T_3} = (0.0270,\ -0.0198,\ 0.0265)$ nm |
| $\boldsymbol{s}_4^{T_1} = (0.0581,\ 0.0427,\ -0.0571)$ nm | $\boldsymbol{s}_4^{T_3} = (-0.0581,\ 0.0427,\ -0.0571)$ nm |
| $\boldsymbol{s}_5^{T_1} = (-0.0187,\ 0.0254,\ 0)$ nm | $\boldsymbol{s}_5^{T_3} = (0.0187,\ 0.0254,\ 0)$ nm |
| $\boldsymbol{s}_6^{T_1} = (0.0187,\ -0.0254,\ 0)$ nm | $\boldsymbol{s}_6^{T_3} = (-0.0187,\ -0.0254,\ 0)$ nm |

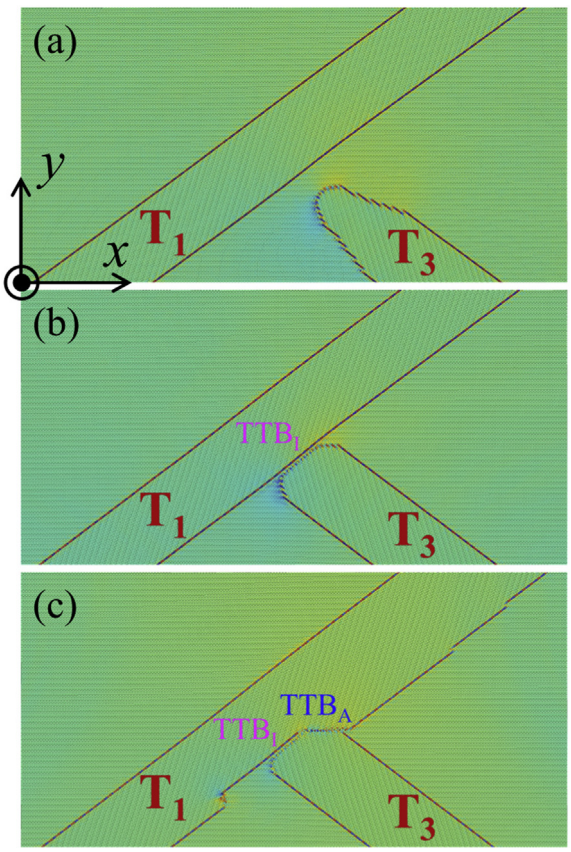


**Fig. 10.** (a) Initial Type II(b) $T_3 \rightarrow T_1$ twin-twin structure. (b) and (c) Final structures under 500 MPa and 700 MPa resolved shear stress with respect to $T_1$ and $T_3$.

$$\mathbf{S}_0' = \begin{pmatrix} -0.35 & 0 & 0 \\ 0 & 0.35 & -0.23 \\ 0 & -0.23 & 0 \end{pmatrix} \text{GPa} \tag{13}$$

When the stress gradually increases from $\mathbf{S_0'}$ to $\mathbf{S_2}$

$$\mathbf{S}_2 = \begin{pmatrix} -0.46 & 0 & 0 \\ 0 & 0.46 & -0.30 \\ 0 & -0.30 & 0 \end{pmatrix} \text{GPa} \tag{14}$$

which generates a resolved shear stress of 500 MPa on the two twin planes, $T_3$ propagates towards $T_1$. It is observed that $TTB_I$ parallel to $(\bar{1}\,0\,1\,2)_M$ plane is formed as $T_3$ is blocked at the coherent twin boundaries (CTB) of $T_1$ (Fig. 10(b)). $TTB_A$ and $TTB_O$ do not form at a shear stress of 500 MPa. When the applied shear stress increases up to 700 MPa, $TTB_A$ is observed as shown in Fig. 10(c). In addition, detwinning of $T_1$ occurs on the obtuse side. This phenomenon could be ascribed to the change in the resolved shear stress on the obtuse side due to the local stress resulted by twinning dislocations associated with $T_3$. In reality, the local stress could be relaxed in different ways, for instance, triggering nucleation and emission of gliding dislocations into the twin $T_1$ (i.e., slip transmission) [53–55]. However, intrinsic limits associated with MD simulations such as small simulation cell (specially a thinner $T_1$ twin) and short simulation period may inhibit such reactions, and the result is a preference of detwinning on the obtuse side. Despite possible artifact, MD simulations of type II(b) interaction reveals similar structural features to these observed in experiments.

We further analyzed the local stress fields in the vicinity of the TTJ. Fig. 11(a)-(c) show the stress fields of $\tau^{T_1}$, $\tau^{T_3}$, and $\tau^b$, respectively. The variations of these three shear stresses on the plane with 1 nm away from the TBs (denoted by the arrowed lines) are shown in Fig. 11(d). $\tau^{T_1}$ and $\tau^{T_3}$ are negative on the acute side. Accordingly, twinning is impeded on the acute side. A negative $\tau_{xy}^{T_3}$ on the obtuse side impedes the glide of TDs associated with the incoming twin $T_3$ towards the encountering twin $T_1$. As a result, nucleation of TDs through the dissociation of the incoming TDs on the coherent twin boundary of the encountering twin $T_1$ is difficult, which prevents the formation of $TTB_A$. These MD simulation results are consistent with the experimental observations. In addition, the shear stress $\tau^b$ on the basal plane is approximately equal to 440 MPa near the twin boundary on the acute side. Such a high stress will facilitate the nucleation and emission of basal <***a***> dislocations inside the encountering twin and consequently relax the local stress to enable growth of the non-equilibrium $TTB_I$ boundary [42,50].

### 4.3. Dynamics process vs. energetics process

From a thermodynamic viewpoint, a lower formation energy of an interface leads to a higher possibility to form and grow the interface. Compared to structural characteristics observed in experiments, molecular statics calculations for TTBs associated with Type II(a) interaction demonstrate a conventional understanding that equilibrium $TTB_O$ is more energetically favorable than equilibrium $TTB_A$ and $TTB_I$. However, for Type II(b) interaction, equilibrium $TTB_A$ with a lower formation energy than other TTBs does not form. The inconsistency points to a dynamic process in creating a boundary. In principle, a boundary bounded two crystals at a certain orientation relation could be non-equilibrium or equilibrium with respect to the formation process. For instance, a boundary formed during annealing is close to equilibrium boundary, while a boundary formed during mechanical deformation is non-equilibrium as a result of dislocations pileup [50,56]. These dislocations generate a long-range stress field, resulting high strain energy in the adjacent crystals. On the other hand, a non-equilibrium boundary tends to relax into an equilibrium

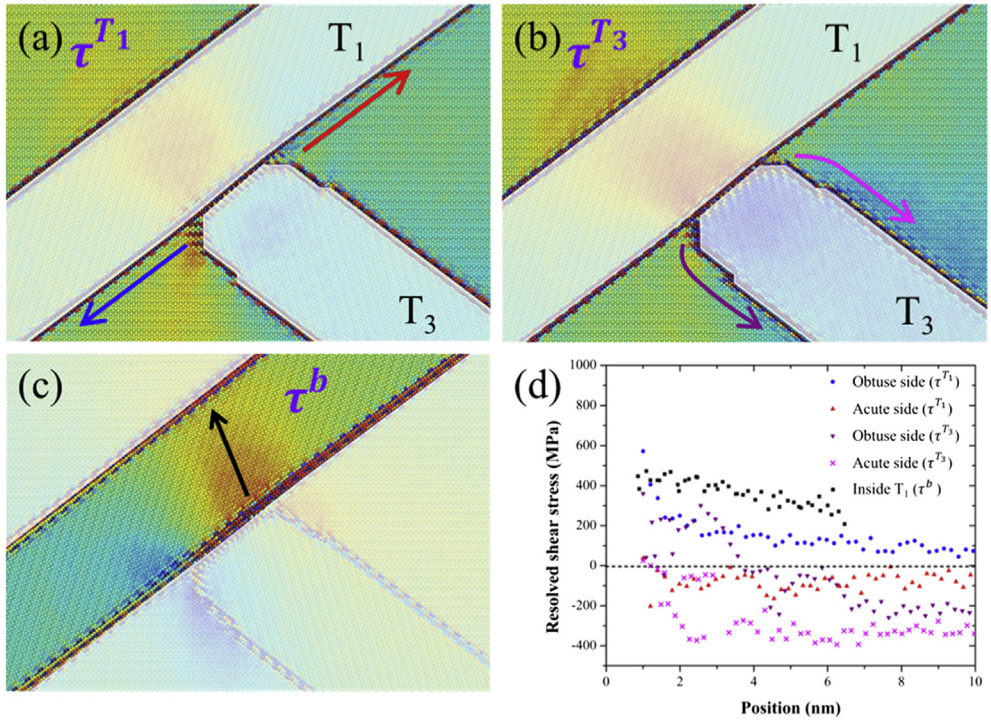


**Fig. 11.** (a)–(c) Stress fields of resolved shear stress $\tau^{T_1}$ and $\tau^{T_3}$ and shear stress $\tau^b$ near Type II(b) TTJ. (d) Variations of $\tau^{T_1}$, $\tau^{T_3}$ and $\tau^b$ on the planes near the TBs along the arrowed lines.

boundary through rearranging boundary dislocations and/or emitting lattice dislocations into the two crystals. As a result, a short-range stress field is localized near the boundary, reducing strain energy in the adjacent crystals while generally increasing formation energy of the boundary [41,42,50]. Therefore, a boundary characterized in a deformed specimen could be a near-equilibrium boundary or a non-equilibrium boundary due to partial relaxation of boundary dislocations.

Dislocations pileup and patterning (associated with forming a non-equilibrium boundary) must precede dynamic relaxation during boundary formation due to deformation. Therefore, the local stress field plays a central role in determining whether dislocations can pile up and pattern to form a boundary. MD simulations demonstrate the importance of local stresses in accounting for the formation of Type II TTJs. For Type II(a) TTJs, both resolved shear stresses associated with two twins have positive values on the obtuse side, speculating preference of $T_1$ and $T_2$ twinning. However, the resolved shear stresses have negative values on the acute side, suggesting impediment of $T_1$ and $T_2$ twinning and $TTB_A$. For Type II(b) TTJs, the resolved shear stresses associated with two twins are negative on the acute side, which impedes twinning on the acute side. On the obtuse side, the resolved shear stress associated with the incoming twin is negative. The result is the impediment of gliding of TDs associated with the incoming twin towards the encountering twin and a decrease in the possibility of TDs nucleation on the coherent twin boundary of the encountering twin through the dissociation of the incoming TDs. In addition, a high shear stress inside the encountering twin facilitates slip transmission for TDs across the twin boundary of the encountering twin, enabling the growth of the non-equilibrium $TTB_I$ boundary.

## 5. Conclusions

Non-cozone twin-twin interactions can be classified into two types, Type II(a) ($T_2 \rightarrow T_1$) and Type II(b) ($T_3 \rightarrow T_1$), according to the crystallography of the two interacting twins. In this work, we characterized the microstructures of non-cozone TTJs according to EBSD results of a deformed pure polycrystalline Mg and studied the twin-twin interaction processes via MD simulations. A statistical analysis of the structures of TTJs from the experiment indicates that for Type II(a) interaction, TTB forms on the obtuse side of the incoming twin, implying that the growth of two twins is favored on the obtuse side while impeded on the acute side. For Type II(b) interaction, incoming twin is blocked by the encountering twin, and the growth of both twins seems impeded. Using MS/MD simulations, we captured the essential structural characteristics of Type II(a) and Type II(b) twin-twin interactions that are consistent with the experimental observations. The simulations accounted for the structural characteristics based on formation energy of equilibrium boundary, dislocation reactions, and local stress fields associated with the formation of TTJs.

## Acknowledgements

Gong, Xu, and Wang acknowledge supports from the US National Science Foundation (NSF) (CMMI-1661686). Jiang thanks the NSF support (CMMI-1462885). The authors acknowledge Dr. Rodney J. McCabe and Dr. Q. Yu for their support on the microstructure characterization. Access to the microscopes at Electron Microscopy Lab at Los Alamos National Laboratories are also acknowledged.

## Appendix

An interface is bonding two crystalline planes in the two twin variants, thus an interface plane is parallel to the two crystalline planes in the two twin variants. Since the two twins are described in the same matrix, the interface plane can also be defined with reference to the matrix. Therefore, the plane of TTBs is firstly

described with reference to the matrix-oriented unit cell. We then described the indices of these crystalline planes in $T_1$-, $T_2$- (or $T_3$-) orientated unit cells.

For a twinning system, the twinning reference frame is set up as: X || the shear direction (SD), Y || the normal of the shear plane (SPN), Z || the normal of the twinning plane (TPN), SPN (**p**) is the cross product of HPN (**m**) and SD (**n**) [17,57,58].

$$Mct = \begin{bmatrix} n_1 & p_1 & m_1 \\ n_2 & p_2 & m_2 \\ n_3 & p_3 & m_3 \end{bmatrix} \tag{A1}$$

For a compound twin, twinning operation is equivalent to a rotation of 180° around the TPN. This rotation matrix ($R_{tw}$) can be obtained as follows:

$$Rtw = \begin{bmatrix} -1 & 0 & 0 \\ 0 & -1 & 0 \\ 0 & 0 & 1 \end{bmatrix} \tag{A2}$$

Then, the indices of a plane *(h, k, i, l)* expressed in crystal coordinate of the twin can be transformed into the Bravais lattice frame of the corresponding parent grain as [59]:

$$\mathbf{P} = \left(M_{3o}^{-1} \cdot \left(M_{ct} \cdot \left(R_{tw} \cdot \left(M_{ct}^{-1} \cdot \left(M_{3o} \cdot ([h\,k\,l] \cdot g^*)^T\right)\right)\right)\right)\right)^T \cdot (g)^{-1} \tag{A3}$$

Similarly, the indices of a direction [*u, v, t, w*] expressed in crystal coordinate of the twin can be transformed into the Bravais lattice frame of the corresponding parent grain as [59]:

$$\mathbf{D} = M_o^{-1} \cdot \left(M_{ct} \cdot \left(R_{tw} \cdot \left(M_{ct}^{-1} \cdot \left(M_o \cdot [u\ v\ w]^T\right)\right)\right)\right) \tag{A4}$$

In the above equations, *c/a* is the axial ratio. $M_{3o}$ enables us to obtain the indices of crystallographic directions expressed in crystal orthonormal coordinate when the Miller indices are given. $M_o$ is the coordinate transformation matrix for directions from crystal orthonormal coordinate to Miller-Bravais system. The metric tensor in direct space and in the reciprocal space is represented by $g$ and $g^*$, respectively. It should be mentioned that all calculations associated with the matrices used are expressed in matrix notation.

## References


[1] E. Aghion, B. Bronfin, Magnesium alloys development towards the 21st century, Materials Science Forum, Trans Tech Publ (2000) 19–30.
[2] I. Polmear, Magnesium alloys and applications, Mater. Sci. Technol. 10 (1) (1994) 1–16.
[3] P.G. Partridge, The crystallography and deformation modes of hexagonal close-packed metals, Metall. Rev. 12 (1) (1967) 169–194.
[4] M.H. Yoo, C.T. Wei, Slip modes of hexagonal-close-packed metals, J. Appl. Phys. 38 (11) (1967) 4317–4322.
[5] J.W. Christian, S. Mahajan, Deformation twinning, Prog. Mater. Sci. 39 (1) (1995) 1–157.
[6] P.W. Bakarian, C.H. Mathewson, Slip and twinning in Magnesium single crystals at elevated temperatures, Transactions of the Metallurgical Society of AIME 152 (1943) 226–254.
[7] A. Chapuis, J.H. Driver, Temperature dependency of slip and twinning in plane strain compressed magnesium single crystals, Acta Mater. 59 (5) (2011) 1986–1994.
[8] R. Sánchez-Martín, M.T. Pérez-Prado, J. Segurado, J. Bohlen, I. Gutiérrez-Urrutia, J. Llorca, J.M. Molina-Aldareguia, Measuring the critical resolved shear stresses in Mg alloys by instrumented nanoindentation, Acta Mater. 71 (2014) 283–292.
[9] W.B. Hutchinson, M.R. Barnett, Effective values of critical resolved shear stress for slip in polycrystalline magnesium and other hcp metals, Scripta Mater. 63 (7) (2010) 737–740.
[10] Z. Wu, W.A. Curtin, The origins of high hardening and low ductility in magnesium, Nature 526 (7571) (2015) 62–67.
[11] R.E. Reed-Hill, A study of the (1011) and (1013) twinning modes in magnesium, Transactions of the American Institute of Mining and Metallurgical Engineers 218 (3) (1960) 554–558.
[12] H. Yoshinaga, R. Horiuchi, Deformation mechanisms in magnesium single crystals compressed in the direction parallel to hexagonal axis, Transactions of the Japan Institute of Metals 4 (1) (1963) 1–8.
[13] Q. Yu, J. Wang, Y. Jiang, R.J. McCabe, N. Li, C.N. Tomé, Twin–twin interactions in magnesium, Acta Mater. 77 (2014) 28–42.
[14] H. El Kadiri, J. Kapil, A.L. Oppedal, L.G. Hector, S.R. Agnew, M. Cherkaoui, S.C. Vogel, The effect of twin–twin interactions on the nucleation and propagation of twinning in magnesium, Acta Mater. 61 (10) (2013) 3549–3563.
[15] S. Xu, M. Gong, X. Xie, Y. Liu, C. Schuman, J.-S. Lecomte, J. Wang, Crystallographic characters of {1122} twin-twin junctions in titanium, Phil. Mag. Lett. (2017) 1–13.
[16] P.A. Juan, C. Pradalier, S. Berbenni, R.J. McCabe, C.N. Tomé, L. Capolungo, A statistical analysis of the influence of microstructure and twin–twin junctions on twin nucleation and twin growth in Zr, Acta Mater. 95 (2015) 399–410.
[17] É. Martin, L. Capolungo, L. Jiang, J.J. Jonas, Variant selection during secondary twinning in Mg–3%Al, Acta Mater. 58 (11) (2010) 3970–3983.
[18] I.J. Beyerlein, J. Wang, M.R. Barnett, C.N. Tome, Double twinning mechanisms in magnesium alloys via dissociation of lattice dislocations, Proc. Royal Soc. A Math Phys Eng. Sci. 468 (2141) (2012) 1496–1520.
[19] D. Ando, J. Koike, Y. Sutou, Relationship between deformation twinning and surface step formation in AZ31 magnesium alloys, Acta Mater. 58 (13) (2010) 4316–4324.
[20] M.R. Barnett, Z. Keshavarz, A.G. Beer, X. Ma, Non-Schmid behaviour during secondary twinning in a polycrystalline magnesium alloy, Acta Materialia 56 (1) (2008) 5–15.
[21] A. Jäger, A. Ostapovets, P. Molnár, P. Lejček, {10-12}-{10-12} Double twinning in magnesium, Phil. Mag. Lett. 91 (8) (2011) 537–544.
[22] Z.-Z. Shi, Y. Zhang, F. Wagner, T. Richeton, P.-A. Juan, J.-S. Lecomte, L. Capolungo, S. Berbenni, Sequential double extension twinning in a magnesium alloy: combined statistical and micromechanical analyses, Acta Mater. 96 (2015) 333–343.
[23] S. Mu, J.J. Jonas, G. Gottstein, Variant selection of primary, secondary and tertiary twins in a deformed Mg alloy, Acta Mater. 60 (5) (2012) 2043–2053.
[24] Q. Yu, Y. Jiang, J. Wang, Tension-compression-tension tertiary twins in coarse-grained polycrystalline pure magnesium at room temperature, Phil. Mag. Lett. 95 (4) (2015) 194–201.
[25] Q. Yu, J. Wang, Y. Jiang, R.J. McCabe, C.N. Tomé, Co-zone {-1012} twin interaction in magnesium single crystal, Materials Research Letters 2 (2) (2014) 82–88.
[26] Q. Yu, J. Zhang, Y. Jiang, Direct observation of twinning–detwinning–retwinning on magnesium single crystal subjected to strain-controlled cyclic tension–compression in [0 0 0 1] direction, Phil. Mag. Lett. 91 (12) (2011) 757–765.
[27] G.-D. Sim, G. Kim, S. Lavenstein, M.H. Hamza, H. Fan, J.A. El-Awady, Anomalous hardening in magnesium driven by a size-dependent transition in deformation modes, Acta Mater. 144 (2018) 11–20.
[28] S. Xu, M. Gong, C. Schuman, J.-S. Lecomte, X. Xie, J. Wang, Sequential {10-12} twinning stimulated by other twins in titanium, Acta Mater. 132 (2017) 57–68.
[29] P.L. Pratt, S.F. Pugh, The movement of twins, kinks, and mosaic walls in zinc, Acta Metall. 1 (2) (1953) 218–222.
[30] E. Roberts, P.G. Partridge, The accommodation around {1012}< 1011> twins in magnesium, Acta Metall. 14 (4) (1966) 513–527.
[31] H. Fu, B. Ge, Y. Xin, R. Wu, C. Fernandez, J. Huang, Q. Peng, Achieving high strength and ductility in magnesium alloys via densely hierarchical double contraction nanotwins, Nano Letters 17 (10) (2017) 6117–6124.
[32] K. Rajan, J.B. Vander Sande, Room temperature strengthening mechanisms in a Co-Cr-Mo-C alloy, J. Mater. Sci. 17 (3) (1982) 769–778.
[33] S. Mahajan, G.Y. Chin, Twin-slip, twin-twin and slip-twin interactions in Co-8 wt.% Fe alloy single crystals, Acta Metall. 21 (2) (1973) 173–179.
[34] Q. Yu, Y. Jiang, J. Wang, Cyclic deformation and fatigue damage in single-crystal magnesium under fully reversed strain-controlled tension–compression in the [10-10] direction, Scripta Mater. 96 (2015) 41–44.
[35] S. Alkan, A. Ojha, H. Sehitoglu, Determination of latent hardening response for FeNiCoCrMn for twin-twin interactions, Acta Mater. 147 (2018) 149–164.
[36] Q. Sun, A. Ostapovets, X. Zhang, L. Tan, Q. Liu, Investigation of twin–twin interaction in deformed magnesium alloy, Phil. Mag. (2017) 1–11.
[37] Q. Sun, X.Y. Zhang, Y. Ren, L. Tan, J. Tu, Observations on the intersection between {10-12} twin variants sharing the same zone axis in deformed magnesium alloy, Mater. Char. 109 (2015) 160–163.
[38] B.M. Morrow, E.K. Cerreta, R.J. McCabe, C.N. Tome, Toward understanding twin–twin interactions in hcp metals: utilizing multiscale techniques to characterize deformation mechanisms in magnesium, Mater. Sci. Eng., A 613 (2014) 365–371.
[39] J. Wang, Q. Yu, Y. Jiang, I.J. Beyerlein, Twinning-associated boundaries in hexagonal close-packed metals, JOM (J. Occup. Med.) 66 (1) (2013) 95–101.
[40] J.P. Hirth, J. Lothe, Theory of Dislocations, second ed., Wiley, New York, 1982.
[41] J. Wang, I.J. Beyerlein, Atomic structures of [0-110] symmetric tilt grain boundaries in hexagonal close-packed (hcp) crystals, Metall. Mater. Trans. 43 (10) (2012) 3556–3569.
[42] M. Gong, J.P. Hirth, Y. Liu, Y. Shen, J. Wang, Interface structures and twinning mechanisms of twins in hexagonal metals, Materials Research Letters (2017)

1–16.
[43] D.M. Barnett, J. Lothe, An image force theorem for dislocations in anisotropic bicrystals, J. Phys. F Met. Phys. 4 (10) (1974) 1618.
[44] A. Serra, D.J. Bacon, A new model for {10-12} twin growth in hcp metals, Philos. Mag. A 73 (2) (1996) 333–343.
[45] L. Capolungo, I.J. Beyerlein, C.N. Tomé, Slip-assisted twin growth in hexagonal close-packed metals, Scripta Mater. 60 (1) (2009) 32–35.
[46] Y. Liu, N. Li, S. Shao, M. Gong, J. Wang, R.J. McCabe, Y. Jiang, C.N. Tome, Characterizing the boundary lateral to the shear direction of deformation twins in magnesium, Nat. Commun. 7 (2016) 11577.
[47] P.B. Price, Nucleation and growth of twins in dislocation-free zinc, Proc. Royal Soc. London Math. Phys. Eng. Sci. 260 (1301) (1961) 251–262.
[48] J. Wang, I.J. Beyerlein, Atomic structures of symmetric tilt grain boundaries in hexagonal close packed (hcp) crystals, Model. Simulat. Mater. Sci. Eng. 20 (2) (2012) 024002.
[49] R. Fullman, J. Fisher, Formation of annealing twins during grain growth, J. Appl. Phys. 22 (11) (1951) 1350–1355.
[50] J.P. Hirth, J. Wang, C.N. Tomé, Disconnections and other defects associated with twin interfaces, Prog. Mater. Sci. 83 (2016) 417–471.
[51] J. Wang, N. Li, A. Misra, Structure and stability of Σ3 grain boundaries in face centered cubic metals, Phil. Mag. 93 (4) (2013) 315–327.
[52] N. Li, J. Wang, A. Misra, X. Zhang, J.Y. Huang, J.P. Hirth, Twinning dislocation multiplication at a coherent twin boundary, Acta Mater. 59 (15) (2011) 5989–5996.
[53] N. Li, J. Wang, J.Y. Huang, A. Misra, X. Zhang, Influence of slip transmission on the migration of incoherent twin boundaries in epitaxial nanotwinned Cu, Scripta Mater. 64 (2) (2011) 149–152.
[54] S. Suri, G. Viswanathan, T. Neeraj, D.-H. Hou, M. Mills, Room temperature deformation and mechanisms of slip transmission in oriented single-colony crystals of an α/β titanium alloy, Acta Mater. 47 (3) (1999) 1019–1034.
[55] J. Wang, A. Misra, R.G. Hoagland, J.P. Hirth, Slip transmission across fcc/bcc interfaces with varying interface shear strengths, Acta Mater. 60 (4) (2012) 1503–1513.
[56] C.D. Barrett, H. El Kadiri, The roles of grain boundary dislocations and disclinations in the nucleation of {102} twinning, Acta Mater. 63 (2014) 1–15.
[57] J.J. Jonas, S. Mu, T. Al-Samman, G. Gottstein, L. Jiang, È. Martin, The role of strain accommodation during the variant selection of primary twins in magnesium, Acta Mater. 59 (5) (2011) 2046–2056.
[58] Z.-Z. Shi, Y. Zhang, F. Wagner, P.-A. Juan, S. Berbenni, L. Capolungo, J.-S. Lecomte, T. Richeton, On the selection of extension twin variants with low Schmid factors in a deformed Mg alloy, Acta Mater. 83 (2015) 17–28.
[59] S. Xu, Crystallographic Analysis of Twin Variant Selection and Twin-Twin Junctions in Commercially Pure Titanium, PhD Thesis, Université de Lorraine, 2017.